Improved corrosion protection of titanium implant material by crystallographic texturing of Sr doped calcium phosphate electrodeposits

Munirathinam, Balakrishnan; Jaladurgam, Nitesh R.; Magesh, J.; Narayanan, Ramaswamy; Mol, Johannes M.C.; Neelakantan, Lakshman

DOI
10.1016/j.tsf.2019.02.010

Publication date
2019

Document Version
Final published version

Published in
Thin Solid Films

Thin Solid Films 675 (2019) 115–121

Contents lists available at ScienceDirect

Thin Solid Films

journal homepage: www.elsevier.com/locate/tsf

Improved corrosion protection of titanium implant material by crystallographic texturing of Sr doped calcium phosphate electrodeposits

Balakrishnan Munirathinam[a,b,*], Nitesh R. Jaladurgam[b,c], J. Magesh[d], Ramaswamy Narayanan[e], Johannes M.C. Mol[a], Lakshman Neelakantan[b]

[a] Department of Materials Science and Engineering Department, Delft University of Technology, Delft, Netherlands
[b] Corrosion Engineering and Materials Electrochemistry Laboratory, Department of Metallurgical and Materials Engineering, Indian Institute of Technology Madras, Chennai, India
[c] Materials Microstructure Division, Department of Physics, Chalmers University of Technology, Gothenburg, Sweden
[d] Department of Physics, Indian Institute of Technology Madras, Chennai, India
[e] School of Mechanical and Building Sciences, VIT University, Chennai, India

ARTICLE INFO

Keywords:
Electrodeposition
Calcium phosphate
X-ray diffraction
Texture
Corrosion resistance

ABSTRACT

Nanocrystalline calcium phosphate (CaP) coatings can provide biocompatibility and corrosion protection to biomaterials upon implementation in the human body. While the long term stability of recently developed coatings in biological environment proves to be challenging, the present work tailors the surface by orienting the growth (crystallographic texturing) of strontium doped CaP coatings in order to increase their corrosion resistance. X-ray diffraction (XRD) as well as selected area electron diffraction patterns from transmission electron microscopy reveal that nanocrystalline CaP crystallizes in hexagonal hydroxyapatite structure preferentially oriented along the *c*-axis. Orientation distribution function obtained from XRD texture studies confirms the presence of a [0001] fiber texture and the estimated texture index indicates the evolution of texture with increasing deposition current density. Polarization studies point out that increasingly textured coatings decrease the corrosion current density by an order of magnitude (from 2.43×10^{-7} to 3.46×10^{-8} A cm^{-2}). Impedance measurements confirm that oriented growth of film renders improved corrosion resistance. This study demonstrates that oriented growth of electrodeposited films strongly improves the corrosion performance of titanium, which can be employed in design and development of highly corrosion resistive implant materials.

1. Introduction

Nanocrystalline calcium phosphate (CaP) coatings have great potential for dental and orthopedic applications as these coatings on medical material provide better biocompatibility and corrosion resistance [1–5]. However, the long term stability of these coatings in biological environment is still challenging matter of concern. Hence, dopants like magnesium, manganese, strontium, fluorine, zinc, carbon, cerium, silver etc., have been incorporated into the lattice of CaP to enhance their biological properties when they are released inside the body. Although the dissolution of CaP coating is an essential requirement for bioactivity behavior as well to improve implant osseointegration, it has some unintended effects. There is a general agreement that the ion dissolution diminishes the stability and increases the potential for loosening of the implant materials. CaP coatings with high stability and low dissolution are favorable for their long-term performance [6]. Also, it is well documented in literature that addition of these dopants improves the corrosion behavior, biocompatibility, osteoinductive and antibacterial activity of coated implant materials [7–11].

In general, hydroxyapatite (HaP) and brushite are the two main CaP phases formed during electrochemical deposition. In electrodeposition, brushite and HaP compete with each other and the evolution of these phases dictates the aforementioned biological properties. HaP, a stable phase, which crystallizes in a hexagonal lattice exhibits better biocompatibility and corrosion resistance than brushite. On the other hand, brushite crystallizes in a monoclinic lattice configuration and shows good resorbing characteristics [6]. To further improve all these characteristics in CaP coatings, isovalent strontium (Sr) doping have been attempted. Strontium can substitute readily in CaP (in HaP or brushite phase) lattice owing to its similar charge to size ratio and ionic radius as calcium [12]. Recently, different research groups have studied

* Corresponding author at: Department of Materials Science and Engineering Department, Delft University of Technology, Delft, Netherlands.
E-mail address: B.Munirathinam@tudelft.nl (B. Munirathinam).

https://doi.org/10.1016/j.tsf.2019.02.010
Received 4 May 2018; Received in revised form 19 January 2019; Accepted 7 February 2019
Available online 08 February 2019
0040-6090/

doping Sr^{2+} ion into CaP lattice to enhance the bone regeneration, bioactivity, osteoblastic cell mineralization and differentiation [13–15]. It has been suggested that better bone cell response is achieved by doping strontium into the HaP nanocrystals [16]. Besides biocompatibility and osteoinductive activity, corrosion of implant material is one of the main concerns from the biomedical perspective. For instance, Gopi et al. [17] studied the corrosion performance of Sr doped HaP coatings with non-doped HaP coatings and showed that Sr doped HaP coatings exhibited lower corrosion current density. Haung et al. [18,19] investigated the corrosion behavior of Sr doped HaP coatings and attributed the higher corrosion resistance to the dense nature and smaller crystallite size of the coatings. These reports comply with examinations of Balyanov et al. [20] showing that nano-crystallites offer high density of grain boundaries for the formation of a stable passive layer and thereby, enhancing the corrosion resistance. Apart from these, corrosion resistance can be further enhanced by orienting the crystallites along the hard axis [21–23]. In principle, electrochemical synthesis facilitates the structural imperfections and growth of oriented films. Herein, we deliberately attempted to crystallographically orient the growth of film by electrodeposition which is expected to improve their corrosion resistance.

In the current work, crystallographic features of Sr-doped CaP coatings electrodeposited at different current densities are extensively investigated and these features are correlated with their electrochemical properties.

2. Experimental

2.1. Electrodeposition of CaP coatings

In order to obtain oriented films, electrodeposition was carried out in a three electrode electrochemical cell coupled to a potentiostat (Gamry Instruments, Reference 600-14083, USA). Ti substrate (grade 2, 99.99%) with the dimension $20 \times 10 \times 1$ mm^3 was used for electrodeposition and the rest of the area was insulated with non-conductive tape. Prior to electrodeposition, substrates were mechanically ground with different grades of SiC emery sheets (grit size 200 to 1000) and ultrasonically cleaned in acetone and dried. Then the substrates were etched for 30 s in a solution containing 5 ml H_2O + 4 ml HNO_3 + 1 ml HF in order to make the surface active and rougher so as to enhance coating adhesion. The electrolytes used for electrodeposition are 18 mM $Ca(NO_3)_2$, 12 mM $NH_4H_2PO_4$ and 2 mM $Sr(NO_3)_2$. An electric heater coupled with a magnetic stirrer (C-MAG HS 4) was used to maintain a bath temperature of 50 °C as well as to stir the electrolyte. The electrodeposition was performed in galvanostatic mode at varying current densities (-0.5, -1.5, -2.5 and -4 mA cm^{-2}) for duration of 30 min. After deposition, samples were washed with de-ionized water and dried at room temperature.

2.2. Surface characterization

X-ray diffraction (XRD) measurements (X'Pert PRO, PANalytical B.V. Amelo, The Netherlands) were carried out using Cu Kα radiation (λ = 1.54 Å), tube voltage 30 kV at a scan speed of 5°/min. Crystallographic analysis was performed using X'Pert HighScore Plus (version 3.0) software and silicon standard was employed for the removal of instrumental broadening. In order to clearly identify the phases formed, the maximum intensity peak of Ti substrate was removed and the unit cell refinement has been carried out using CELREF software [24]. Bulk texture studies were carried out using XRD in reflection geometry with a standard four circle goniometer. X-ray poles were collected at a particular 2θ by measuring the intensity as the sample is rotated through 360° at different tilting angles ranging from 0 to 70°. MTEX Matlab toolbox was used to generate orientation distribution function (ODF) and inverse pole figures [25–27]. The surface morphology of the coatings was studied using a field emission scanning electron microscope (FE-SEM FEI Quanta FEG 400). Contact angle measurements were carried out on the electrodeposited surfaces using a contact angle measurement system (Easy Drop, KRUSS, Germany) with distilled water at ambient conditions. A water droplet (3 µl) was dispensed onto the surface with a syringe and the digital images of the droplet silhouette were captured with a CCD camera within 10 s after wetting. Morphology and composition of the electrodeposits were characterized using a transmission electron microscope (TEM, Philips CM12 - EDAX). The electrodeposits were scraped from the Ti substrate and transferred to the carbon coated copper mesh for TEM characterization.

2.3. Electrochemical characterization

A potentiostat (interfaced with computer and the softwares, Gamry framework and Gamry Echem analyst (model: Reference 600-14083)) was employed to carry out the potentiodynamic polarization and electrochemical impedance spectroscopy (EIS) measurements. Electrolyte used for the measurements is isotonic saline solution of 0.9% NaCl which has ion content similar to that of human body fluids. A conventional three electrode setup is employed for the measurements with saturated calomel electrode (SCE) as reference electrode, graphite as counter electrode and deposited sample as working electrode. Prior to the electrochemical measurements, the samples were immersed in the electrolyte for a time period of 2 h in order to attain a stable open circuit potential (OCP). After ensuring a stable OCP, potentiodynamic polarization measurements were carried out by ramping the potential from -0.35 to -1.0 V_{SCE} at a scan rate of 1 mV s^{-1}. EIS was performed at OCP by sweeping the frequency from 0.1 MHz to 10 mHz using an AC perturbation signal of amplitude10 mV (rms). All the potentials reported here are with respect to SCE.

3. Results and discussion

3.1. Crystallographic features of the electrodeposits

To analyze the crystallinity of CaP deposits formed at different current densities, XRD measurements were performed and resultant diffractograms are shown in Fig. 1. The figure reveals all the crystallographic features of deposition kinetics. At lower deposition current density (-0.5 mA cm^{-2}), the thickness of the deposits is relatively small resulting in dominance of the Ti substrate peak. The electrodeposits exhibits mixed brushite and HaP phases which is revealed from

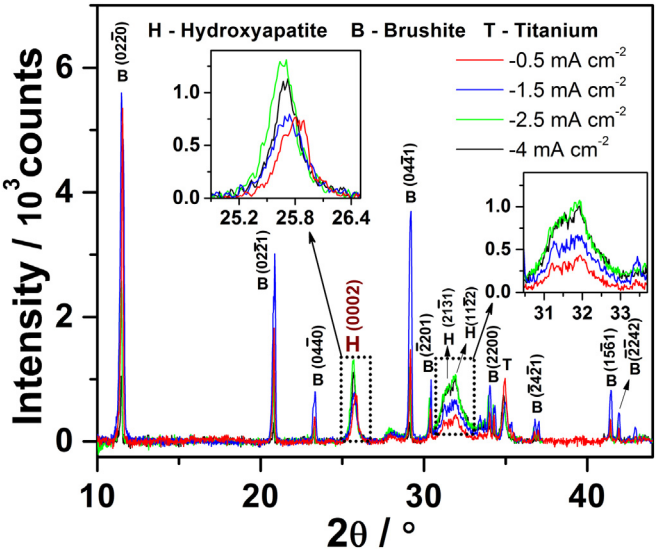

Fig. 1. XRD pattern of the CaP deposits obtained at different current densities.

Table 1
Crystallographic features of the coatings deposited at different current densities.

Current density ($mA\,cm^{-2}$)	Lattice parameter (Å)			Average crystallite size, *t*, (nm)		Texture index (no unit)	Volume of fiber
	HaP		Brushite	HaP	Brushite	HaP	[0001] orientation (in % with 15° degree of freedom)
	$a = b$	c					
−0.5	9.4451 ± 0.0652	6.9122 ± 0.0112	a = 6.3740 ± 0.0049 b = 15.1939 ± 0.0032 c = 5.8132 ± 0.0047	42 ± 8	72 ± 5	2.48	18.21
−1.5	9.4436 ± 0.0504	6.9143 ± 0.0082	a = 6.3737 ± 0.0022 b = 15.1984 ± 0.0015 c = 5.8163 ± 0.0017	36 ± 4	66 ± 6	2.50	18.36
−2.5	9.4652 ± 0.0464	6.9081 ± 0.0020	a = 6.3695 ± 0.0031 b = 15.1846 ± 0.0017 c = 5.8164 ± 0.0025	28 ± 4	53 ± 6	3.44	19.44
−4	9.4857 ± 0.0558	6.8662 ± 0.0059	a = 6.4129 ± 0.0461 b = 15.2056 ± 0.0127 c = 5.7894 ± 0.0359	22 ± 5	49 ± 2	3.59	20.30

the large number of sharp crystalline peaks in the diffraction pattern. With further increase in current density ($-1.5\,mA\,cm^{-2}$), the amount of brushite phase increases along with concomitant increase of film thickness inferred by decrease of Ti substrate peak. At higher current densities (-2.5 and $-4\,mA\,cm^{-2}$), HaP evolves at the expense of the brushite phase. However, the reemergence of the Ti peak at $-4\,mA\,cm^{-2}$ signifies a decrease of the thickness of the film. The suggested thickness variation has to be further ascertained by other technique and will be discussed quantitatively in forthcoming section. The mean crystallite size (t) of the HaP and brushite phases were estimated using well-known Scherer equation,

$$t = (0.9\lambda/B\cos\theta) \quad (1)$$

where, λ is the wavelength of X-rays (Cu Kα - 1.54 Å), B is the line width at half maximum (in radian) and θ is the diffraction angle. The corresponding reflections of HaP and brushite phases observed are chosen for analysis of the peak width by fitting all of them using Pseudo-Voigt profile function and the estimated average crystallite size of all samples is shown in Table 1. It is also important to note that the crystallite size of both phases decreases with current density. This is presumably attributed to the generation of hydroxyl ions during the electrodeposition. More number of hydroxyl groups is produced at higher current density which offers an ample supply of co-ordinate sites for complexation with calcium ions. This facilitates the extensive amount of nuclei generation of the cathodic surface, thereby resulting in smaller crystallite size [22]. Furthermore, the refined lattice parameter a, b and c of the respective phases shown in Table 1 varies with the deposition current density. Despite the fact that the lattice parameter a (and b) varies only in the third order, the parameter c manifestly decreased with increase in deposition current density. Apparently, the change in lattice parameter is ascribed to the lattice distortion due to the stresses accumulated in the deposited film which occurred concurrently with reduction in crystallite size for HaP and brushite phases. This observation was in accordance with the earlier reports [28,29].

3.2. Bulk texture studies and mechanism of texture evolution

Remarkably, in all the coatings, non-random orientation (texture) of HaP crystallites are observed where (0002) reflection exhibits higher intensity than conventional ($11\bar{2}2$) reflection. To gain further insights into this aspect, bulk texture studies using XRD were performed. Visualization of texture was done through inverse pole figures and ODF sections as shown in Fig. 2a–d. Inverse pole figures (Fig. 2a–b) confirmed the oriented growth of HaP crystallites in [0001] direction with respective to crystal co-ordinates. This can be deciphered from the

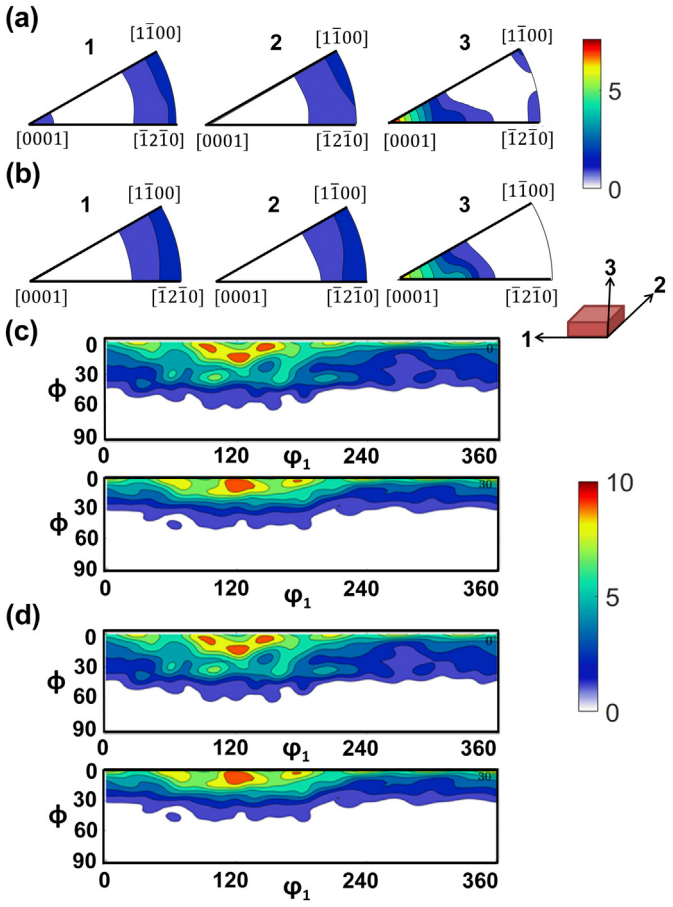

Fig. 2. a) & b) Inverse pole figures for coatings deposited at -0.5 and $-4\,mA\,cm^{-2}$ and the axes 1 and 2 represent the directions parallel to coating surface whereas the axis 3 denotes the direction perpendicular to coating. c) & d) ODF sections for coatings deposited at -0.5 and $-4\,mA\,cm^{-2}$.

increase in diffraction intensity at [0001] direction with current density for sample direction 3 (normal to the substrate). Three dimensional representation of texture using ODF aptly reveals the presence of fiber texture in φ_2 sections of 0° and 30° shown in Fig. 2c–d. The texture index and volume fraction (with tolerance of 15°) of fiber components (Table 1) obtained using ODF section increase with current density ascertaining the fact that fibers are strengthened at higher current densities. In principle, the evolution of phases and c-axis texturing can

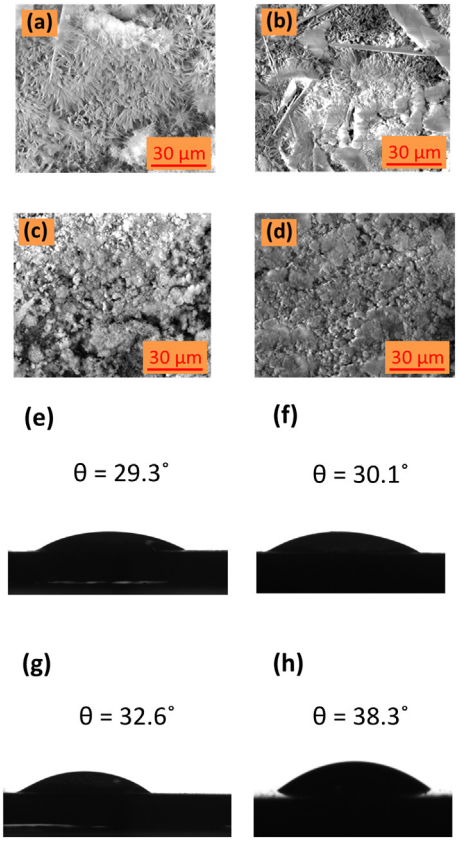

Fig. 3. SEM micrographs of the coatings deposited at a) −0.5, b) −1.5, c) −2.5 and d) −4 mA cm^{-2}. Contact angle of the coatings deposited at e) −0.5, f) −1.5, g) −2.5 and h) −4 mA cm^{-2}.

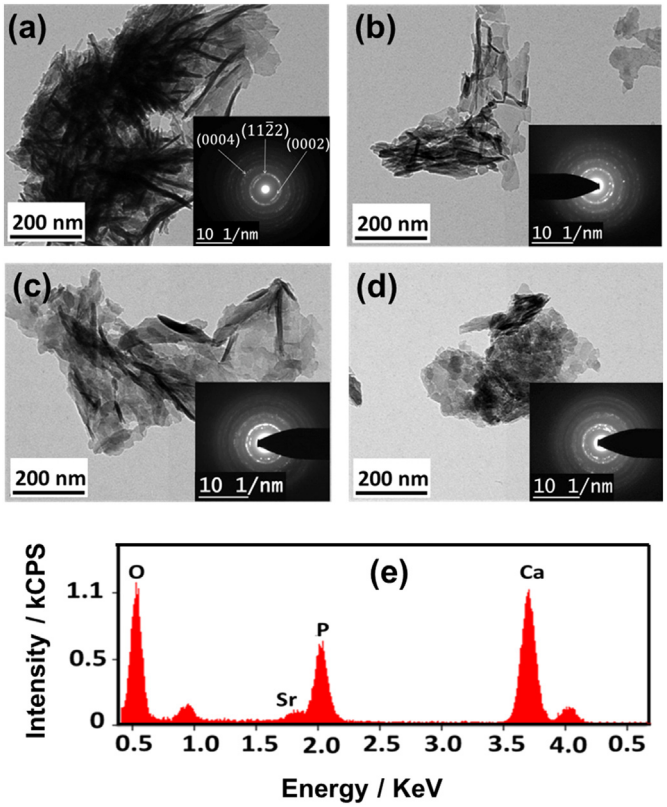

Fig. 4. TEM micrographs of the coatings deposited at a) −0.5, b) −1.5, c) −2.5 and d) −4 mA cm^{-2}. Inset is the corresponding SAED pattern (left). e) EDS analysis of powder scrapped from the coating.

be understood from the lattice strain and hydroxyl group evolution with current density. At lower current densities where hydrogen evolution is minimal, Ti and HaP hexagonal lattice mismatch drives CaP to form the distorted monoclinic phase (brushite). However, at higher current densities where hydrogen evolution is maximal, the trapped hydrogen bubbles bounds the ion loosely, reducing the lattice mismatch favoring the HaP phase formation preferentially. These adsorbed gas bubbles affect the mass transport process establishing a concentration gradient of OH groups along the [0001] direction altering the growth of HaP direction [30,31]. As a result, the aligned crystallites will grow faster than randomly oriented crystallites. This is because of the piling of OH groups which act as 'channels' facilitating OH diffusion and incorporation into the neighboring regions. In this manner, [0001] fiber texture evolves in *c*-axis direction with increasing current density.

3.3. Wettability, surface morphology and local texture of the electrodeposits

SEM micrographs shown in Fig. 3a–d reveal that the electrodeposited coatings form a dense flake- and plate-like structure. Nanocrystalline flake-like morphology evolves into plate or particle like structure upon increasing the deposition current density. However, as all the SEM micrographs are shown at the same magnification, the mixed particle and plate like morphology was not visible. The cross sectional SEM (not shown in figure) micrographs revealed that the thickness of the film increases upon varying the current density from −0.5 to −2.5 mA cm^{-2} (5 µm to 12 µm). But at the highest current density (−4 mA cm^{-2}), the thickness of the film reduces (10 µm), affirming the XRD observation. At higher current density, the rate of hydrogen evolution increases on the surface of the electrode. The increase hydrogen bubbles accumulating at the cathodic surface reduce the precipitation of calcium phosphate on the cathodic surface leading to decrease of thickness of the deposited film. The contact angle of the corresponding morphological structures was recorded (Fig. 3e–h) and the angle values obtained are in the range of 29° to 40°. The rough nano-structure endows the electrodeposits with more hydrophilic character but it is clear that significant difference in the contact angle is not observed among the samples.

To further ascertain the nanocrystalline morphology of the electrodeposits, TEM micrographs (Fig. 4a–d) were recorded from the deposit powder scraped from the titanium substrate. TEM examination revealed that flake-like morphology dominates at lower current densities whilst a plate-like morphology is observed at higher current densities. EDS analysis (Fig. 4e) showed the pronounced peaks of Ca, P, Sr and O confirming the presence of Sr-doped CaP coatings. From the EDS analysis, the molar ratio of (Ca + Sr)/P are in the range of 1.45 to 1.65 for varying current densities. The results suggest that electrodeposits are calcium deficient with low Sr ion (1 to 2 at.%) incorporation. Strontium ion substitutes the calcium lattice in CaP phase as they have close ionic radius (Sr - 1.13 Å and Ca - 0.99 Å) with the calcium ion causing lattice deformation of the crystal. Incorporation of Sr^{2+} into CaP phase not only has activates the osteoblasts and improves bone mineralization but also influences the chemical properties of CaP phases. For instance, Christoffersen et al., [32] demonstrated that Sr substitution in selected sites of Ca in HaP phase alters the dissolution behavior and growth of HaP under in-vitro conditions. On the other hand, in the brushite phase, most Ca sites are replaced by Sr due to the smaller coordination parameters of Sr atoms [33].

Selected area electron diffraction (SAED) pattern shows that the width of ring pattern increases with current density implying reduction in the size of nano-crystallites. Also, it is interesting to note that an arc-like pattern observed for the (0002) facet ascertains the local texture of the electrodeposits.

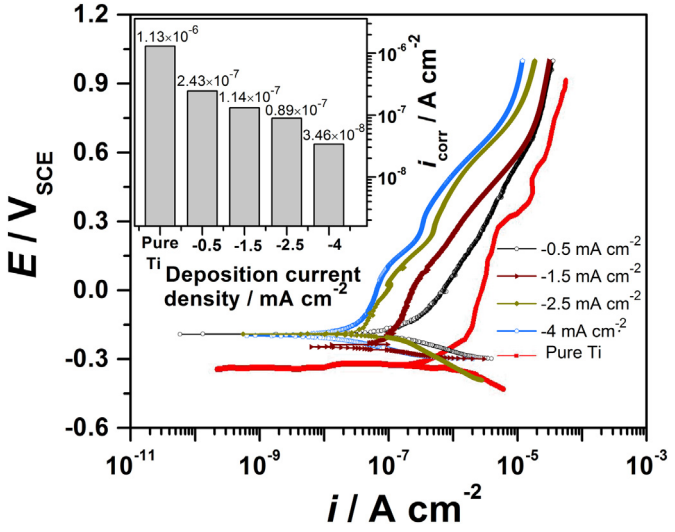

Fig. 5. Polarization curves of coatings recorded in 0.9% NaCl medium. Inset is i_{corr} values estimated using Tafel extrapolation.

3.4. Potentiodyanamic polarization studies

In order to ascertain the role of texture on the corrosion behavior of oriented coatings, potentiodynamic polarization measurements were performed in 0.9% NaCl medium as shown in Fig. 5. It is clearly seen from the anodic branch that all the samples exhibit a wide passive range. The corrosion current density, i_{corr}, was measured for all coatings by Tafel extrapolation [34]. It can be seen that the coated samples exhibits lower i_{corr} value compared to those for bare titanium substrate indicating the higher corrosion resistance of the coated samples. Although the anodic polarization curves exhibit wide passive behavior, a decrease in i_{corr} by an order of magnitude (from 2.43×10^{-7} to 3.46×10^{-8} A cm^{-2}) is observed with increasing deposition current density as shown as inset in Fig. 5. From the crystallographic orientation perspective, the coating with a higher amount of [0001] fiber texture will have higher binding energy of surface atoms. As a consequence, the total energy involved in the resistance to dissolution is higher for such low index plane [35]. Since the texture index and fiber fraction increases with deposition current density, a higher number of (0002) facets are exposed to the electrolyte, resulting in lower charge transfer providing increased protection to the substrate. Furthermore, smaller crystallites exposed to the electrolyte offer more grain boundary area where the distribution of equivalent anodic current occurs concurrent with the reduction of cathodic current due to decreasing of the cathodic area (interior of crystallite). Thus, the corrosion reaction kinetics are reduced with decreasing crystallite size showing lower i_{corr}. It has been reported that doped CaP coatings on titanium substrate exhibits i_{corr} values merely in the order of 10^{-5} to 10^{-6} A cm^{-2} [18,19,36,37]. Furthermore, Suman et al. [38] and Dehestani et al. [39] affirmed that nanocrystalline randomly oriented HaP coatings with and without dopant act as a barrier to the transport of electrons and ions between substrate and the electrolyte, exhibiting i_{corr} values in the order of 10^{-6} A cm^{-2}. From the viewpoint of varying thickness, it was reported in the earlier work [40] that the non-textured film whose thickness varied by varying the deposition current density have similar magnitude of i_{corr}, and it was highlighted that thickness variation (15 to 20 μm) obtained at different deposition conditions did not decrease the i_{corr}, significantly. At this point, it is worth highlighting that for sample with higher texture index, i_{corr} value in the order of 10^{-8} A cm^{-2}, implies that texture predominates the effect of crystallite size and thickness and hence, the observed range confirms that texture plays strong role in the electrochemical behavior, enhancing the corrosion resistance of the titanium surfaces.

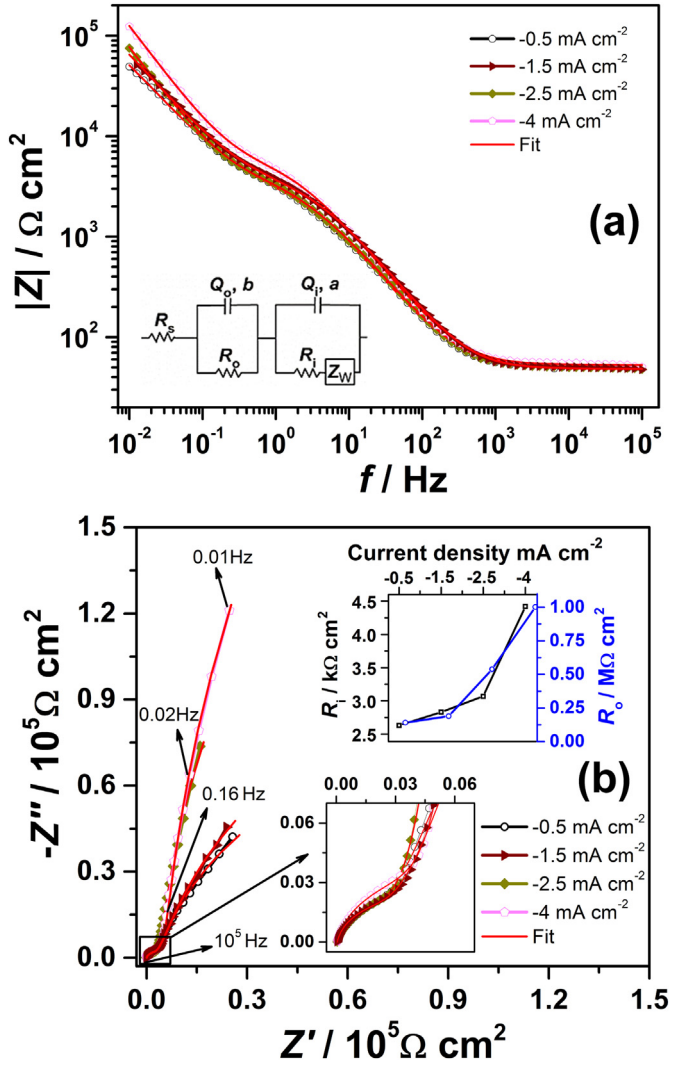

Fig. 6. a) Bode magnitude plot and equivalent circuit used to model experimental data is shown in the inset. b) Nyquist spectra of coatings recorded in 0.9% NaCl medium and inset is the extracted R_i and R_o values.

3.5. EIS analysis

To gain further insight in the electrochemical behavior of the textured coatings, EIS measurements were performed in 0.9% NaCl medium. Bode magnitude plots shown in Fig. 6a demonstrate the presence of two relaxation features over the frequency range scanned. The first time constant observed in the intermediate frequency region corresponds to an outer porous structure and the second time constant observed in the lower frequency domain is pertinent to an inner compact layer. Nonetheless, there is no marked difference noted at very high frequency profiles which is related to the solution resistance. The relaxation features detected in coating/electrolyte interface were also interpreted using Nyquist plots shown in Fig. 6b. It is important to note that the higher frequency domain exhibited a capacitive semicircle whereas linear behavior is observed in the lower frequency region. To account for this dual relaxation phenomenon, an equivalent circuit with two time constants (shown as inset in Fig. 6a) is proposed. In this circuit, R_s is the solution resistance, R_i and R_o are the resistance of the inner charge transfer and outer layer, Z_W is the Warburg impedance which occurs due to transport of ions under the influence of concentration gradient, Q_i and Q_o are the constant phase element (CPE) of the inner and outer layer with exponents a and b. CPE is used instead of capacitance due to distribution of relaxation invoked by interfacial

Table 2
Impedance parameters extracted from the equivalent circuit.

Current density (mA cm^{-2})	R_s (Ω cm^2)	Q_i (μΩ^{-1} s^a cm^{-2})	a	R_i (kΩ cm^2)	Q_o (μΩ^{-1} s^b cm^{-2})	b	R_o (MΩ cm^2)	Z_W (kΩ s$^{-0.5}$ cm^2)	χ^2 (10^{-3})
−0.5	49.07	37.81	0.83	2.63	242.7	0.87	0.14	1.99	3.63
−1.5	47.32	23.53	0.86	2.831	203.0	0.89	0.18	2.63	4.02
−2.5	48.68	34.10	0.83	3.07	232.9	0.93	0.53	2.21	1.86
−4	52.85	25.75	0.86	4.42	131.5	0.94	1.01	2.18	3.54

heterogeneity. The impedance of CPE is described as $Z_{CPE} = [Q(j\omega)^{\alpha}]^{-1}$, where Q and α are the CPE parameters and $j\omega$ is the complex variable for sinusoidal perturbations with $\omega = 2\pi f$ [41]. The extracted impedance parameters are summarized in Table 2. The fitted results of experimental impedance spectra are in good match exhibiting low chi square values in the order of 10^{-3}. It can be seen that R_o values are three orders of magnitude higher than that of R_i (shown as inset in Fig. 6b). While R_i and R_o increase with deposition current density, at higher current densities where texture is favored an order of increment in R_o is observed. This is due to the oriented growth of HaP crystallites which results in lower ionic dissolution rates, exhibiting higher impedance. Moreover, increase in Z_W with deposition current density is observed implying the blocking nature of the deposits formed. These results substantiates with the very low i_{corr} values observed in potentiodynamic polarization tests.

In the light of the present work, it is noteworthy that highly textured deposits enhance the corrosion resistance significantly. This investigation could be a way forward to unravel the effect of crystallographic texture on the adhesion and cell proliferation functionality of osteoblast cultured on CaP deposits.

4. Conclusions

In summary, nanocrystalline Sr doped CaP coatings were synthesized at different current densities and the influence of crystallographic features on the corrosion behavior is evaluated. Crystallographic studies suggest that higher current densities favor the HaP phase with [0001] fiber texture. The increase of fiber texture decreases i_{corr} by an order of magnitude (from 2.43×10^{-7} to 3.46×10^{-8} A cm^{-2}) due to a higher dissolution resistance of (0002) facets. Consequently, it also increased the outer layer resistance by an order of magnitude (from 0.14 to 1 MΩ cm^2) implying that textured HaP crystallites strongly enhances the corrosion resistance of the titanium substrate. The potential to introduce crystallographic texture in the coatings by fine control of deposition current density makes electrodeposition a well-designed electrochemical processing technique for the deposition of CaP coatings for biomaterials with enhanced corrosion performance.

Acknowledgements

We would like to acknowledge Dr. Anand Krishna Kanjarla for his scientific discussion in texture analysis. BM acknowledges Mrs. Agnieszka Kooijman for her technical assistance in carrying out contact angle measurements.

References

[1] X. Liu, P.K. Chu, C. Ding, Surface modification of titanium, titanium alloys, and related materials for biomedical applications, Mater. Sci. Eng. R. Rep. 47 (2004) 49–121, https://doi.org/10.1016/j.mser.2004.11.001.
[2] G. Liu, S. Tang, J. Hu, Y. Zhang, Y. Wang, F. Liu, Corrosion behavior of micro-arc oxidized magnesium with calcium phosphate coating in flowing simulated body fluids, J. Electrochem. Soc. 162 (2015) C426–C432, https://doi.org/10.1149/2.0141509jes.
[3] S.-H. Chen, W.-L. Tsai, P.-C. Chen, A. Fang, W.-C. Say, Influence of applied voltages on mechanical properties and in-vitro performances of electroplated hydroxyapatite coatings on pure titanium, J. Electrochem. Soc. 163 (2016) D305–D308, https://doi.org/10.1149/2.1001607jes.
[4] C.-I. Jo, Y.-H. Jeong, H.-C. Choe, W.A. Brantley, Hydroxyapatite precipitation on nanotubular films formed on Ti-6Al-4V alloy for biomedical applications, Thin Solid Films 549 (2013) 135–140, https://doi.org/10.1016/j.tsf.2013.09.095.
[5] A. Vladescu, D.M. Vranceanu, S. Kulesza, A.N. Ivanov, M. Bramowicz, A.S. Fedonnikov, M. Braic, I.A. Norkin, A. Koptyug, M.O. Kurtukova, M. Dinu, I. Pana, M.A. Surmeneva, R.A. Surmenev, C.M. Cotrut, Influence of the electrolyte's pH on the properties of electrochemically deposited hydroxyapatite coating on additively manufactured Ti64 alloy, Sci. Rep. 7 (2017) 1–20, https://doi.org/10.1038/s41598-017-16985-z.
[6] R. Narayanan, S.K. Seshadri, T.Y. Kwon, K.H. Kim, Calcium phosphate-based coatings on titanium and its alloys, J. Biomed. Mater. Res. - Part B Appl. Biomater. 85 (2008) 279–299, https://doi.org/10.1002/jbm.b.30932.
[7] H.R. Bakhsheshi-Rad, E. Hamzah, M. Daroonparvar, R. Ebrahimi-Kahrizsangi, M. Medraj, In-vitro corrosion inhibition mechanism of fluorine-doped hydroxyapatite and brushite coated Mg-Ca alloys for biomedical applications, Ceram. Int. 40 (2014) 7971–7982, https://doi.org/10.1016/j.ceramint.2013.12.147.
[8] A.Z. Alshemary, A.E. Pazarceviren, A. Tezcaner, Z. Evis, Mesoporous strontium doped nano sized sulphate hydroxyapatite as a novel biomaterial for bone tissue applications, RSC Adv. 6 (2016) 68058–68071, https://doi.org/10.1039/C6RA16809D.
[9] H.R. Bakhsheshi-Rad, E. Hamzah, M. Kasiri-Asgarani, S. Jabbarzare, N. Iqbal, M.R. Abdul Kadir, Deposition of nanostructured fluorine-doped hydroxyapatite-polycaprolactone duplex coating to enhance the mechanical properties and corrosion resistance of Mg alloy for biomedical applications, Mater. Sci. Eng. C 60 (2016) 526–537, https://doi.org/10.1016/j.msec.2015.11.057.
[10] M. Yazici, A.E. Gulec, M. Gurbuz, Y. Gencer, M. Tarakci, Biodegradability and antibacterial properties of MAO coatings formed on Mg-Sr-Ca alloys in an electrolyte containing Ag doped hydroxyapatite, Thin Solid Films 644 (2017) 92–98, https://doi.org/10.1016/J.TSF.2017.10.033.
[11] A. Vladescu, C. Mihai Cotrut, F. Ak Azem, M. Bramowicz, I. Pana, V. Braic, I. Birlik, A. Kiss, M. Braic, R. Abdulgader, R. Booysen, S. Kulesza, T.K. Monsees, Sputtered Si and Mg doped hydroxyapatite for biomedical applications, Biomed. Mater. 13 (2018), https://doi.org/10.1088/1748-605X/aa9718.
[12] J. Terra, E.R. Dourado, J.-G. Eon, D.E. Ellis, G. Gonzalez, A.M. Rossi, The structure of strontium-doped hydroxyapatite: an experimental and theoretical study, Phys. Chem. Chem. Phys. 11 (2009) 568–577, https://doi.org/10.1039/B802841A.
[13] C. Capuccini, P. Torricelli, F. Sima, E. Boanini, C. Ristoscu, B. Bracci, G. Socol, M. Fini, I.N. Mihailescu, A. Bigi, Strontium-substituted hydroxyapatite coatings synthesized by pulsed-laser deposition: in vitro osteoblast and osteoclast response, Acta Biomater. 4 (2008) 1885–1893, https://doi.org/10.1016/j.actbio.2008.05.005.
[14] G.X. Ni, B. Shu, G. Huang, W.W. Lu, H.B. Pan, The effect of strontium incorporation into hydroxyapatites on their physical and biological properties, J. Biomed. Mater. Res. - Part B Appl. Biomater. 100 B (2012) 562–568, https://doi.org/10.1002/jbm.b.31986.
[15] R. Drevet, H. Benhayoune, Pulsed electrodeposition for the synthesis of strontium-substituted calcium phosphate coatings with improved dissolution properties, Mater. Sci. Eng. C 33 (2013) 4260–4265, https://doi.org/10.1016/j.msec.2013.06.019.
[16] C. Capuccini, P. Torricelli, E. Boanini, M. Gazzano, R. Giardino, A. Bigi, Interaction of Sr-doped hydroxyapatite nanocrystals with osteoclast and osteoblast-like cells, J. Biomed. Mater. Res. Part A. 89A (2009) 594–600, https://doi.org/10.1002/jbm.a.31975.
[17] D. Gopi, N. Murugan, S. Ramya, E. Shinyjoy, L. Kavitha, Ball flower like manganese, strontium substituted hydroxyapatite/cerium oxide dual coatings on the AZ91 Mg alloy with improved bioactive and corrosion resistance properties for implant applications, RSC Adv. 5 (2015) 27402–27411, https://doi.org/10.1039/C5RA03432A.
[18] Y. Huang, Q. Ding, X. Pang, S. Han, Y. Yan, Corrosion behavior and biocompatibility of strontium and fluorine co-doped electrodeposited hydroxyapatite coatings, Appl. Surf. Sci. 282 (2013) 456–462, https://doi.org/10.1016/j.apsusc.2013.05.152.
[19] Y. Huang, H. Zeng, X. Wang, D. Wang, Corrosion resistance and biocompatibility of SrHAp/ZnO composite implant coating on titanium, Appl. Surf. Sci. 290 (2014) 353–358, https://doi.org/10.1016/j.apsusc.2013.11.082.
[20] A. Balyanov, J. Kutnyakova, N.A. Amirkhanova, V.V. Stolyarov, R.Z. Valiev, X.Z. Liao, Y.H. Zhao, Y.B. Jiang, H.F. Xu, T.C. Lowe, Y.T. Zhu, Corrosion resistance of ultra fine-grained Ti, Scr. Mater. 51 (2004) 225–229, https://doi.org/10.1016/j.scriptamat.2004.04.011.
[21] Z. Hong, L. Luan, S.B. Paik, B. Deng, D.E. Ellis, J.B. Ketterson, A. Mello, J.G. Eon, J. Terra, A. Rossi, Crystalline hydroxyapatite thin films produced at room temperature - an opposing radio frequency magnetron sputtering approach, Thin Solid Films 515 (2007) 6773–6780, https://doi.org/10.1016/j.tsf.2007.02.089.
[22] B. Munirathinam, L. Neelakantan, Role of crystallographic texture and crystallinity on the electrochemical behavior of nanocrystalline Sr doped calcium phosphate

coatings, J. Electrochem. Soc. 163163 (2016) 336–343, https://doi.org/10.1149/2.1411607jes.
[23] Y. Raghupathy, A. Kamboj, M.Y. Rekha, N.P. Narasimha Rao, C. Srivastava, Copper-graphene oxide composite coatings for corrosion protection of mild steel in 3.5% NaCl, Thin Solid Films 636 (2017) 107–115, https://doi.org/10.1016/j.tsf.2017.05.042.
[24] B. Bochu, Basic Demonstration of CELREF Unit-Cell Refinement Software on a Multiphase System, (2009), pp. 1–10 http://www.inpg.fr/LMGP/.
[25] H.-J. Bunge, 3 - orientation distributions, in: H.-J. Bunge (Ed.), Texture Anal. Mater. Sci, Butterworth-Heinemann, 1982, pp. 42–46, , https://doi.org/10.1016/B978-0-408-10642-9.50008-8.
[26] R. Hielscher, H. Schaeben, A novel pole figure inversion method: Specification of the MTEX algorithm, J. Appl. Crystallogr. 41 (2008) 1024–1037, https://doi.org/10.1107/S0021889808030112.
[27] F. Bachmann, R. Hielscher, H. Schaeben, Texture analysis with MTEX – free and open source software toolbox, Solid State Phenom. 160 (2010) 63–68, https://doi.org/10.4028/www.scientific.net/SSP.160.63.
[28] M.I. Ahmad, S.S. Bhattacharya, Size effect on the lattice parameters of nanocrystalline anatase, Appl. Phys. Lett. 95 (2009) 191906, , https://doi.org/10.1063/1.3261754.
[29] Y. Gupta, P. Arun, A.A. Naudi, M.V. Walz, E.A. Albanesi, Grain size and lattice parameter's influence on band gap of SnS thin nano-crystalline films, Thin Solid Films 612 (2016) 310–316, https://doi.org/10.1016/j.tsf.2016.05.056.
[30] M. Manso, C. Jiménez, C. Morant, P. Herrero, J.M. Martínez-Duart, Electrodeposition of hydroxyapatite coatings in basic conditions, Biomaterials 21 (2000) 1755–1761 https://doi.org/10.1016/S0142-9612(00)00061-2.
[31] N. Eliaz, T.M. Sridh, Electrocrystallization of hydroxyapatite and its dependence on solution conditions, Cryst. Growth Des. 8 (2008) 3965–3977, https://doi.org/10.1021/cg800016h.
[32] J. Christoffersen, M.R. Christoffersen, N. Kolthoff, O. Bärenholdt, Effects of strontium ions on growth and dissolution of hydroxyapatite and on bone mineral detection, Bone 20 (1997) 47–54, https://doi.org/10.1016/S8756-3282(96)00316-X.
[33] E. Rokita, C. Hermes, H.F. Nolting, J. Ryczek, Substitution of calcium by strontium within selected calcium phosphates, J. Cryst. Growth 130 (1993) 543–552, https://doi.org/10.1016/0022-0248(93)90543-6.
[34] E. McCafferty, Validation of corrosion rates measured by the Tafel extrapolation method, Corros. Sci. 47 (2005) 3202–3215, https://doi.org/10.1016/j.corsci.2005.05.046.
[35] G.L. Song, R. Mishra, Z. Xu, Crystallographic orientation and electrochemical activity of AZ31 Mg alloy, Electrochem. Commun. 12 (2010) 1009–1012, https://doi.org/10.1016/j.elecom.2010.05.011.
[36] K. Kung, T. Lee, T. Lui, Bioactivity and corrosion properties of novel coatings containing strontium by micro-arc oxidation, J. Alloys Compd. 508 (2010) 384–390, https://doi.org/10.1016/j.jallcom.2010.08.057.
[37] Y.-H. Jeong, H.-C. Choe, W.A. Brantley, Silicon-substituted hydroxyapatite coating with Si content on the nanotube-formed Ti–Nb–Zr alloy using electron beam-physical vapor deposition, Thin Solid Films 546 (2013) 189–195, https://doi.org/10.1016/j.tsf.2013.05.130.
[38] S. Singh, V.K. Meena, M. Sharma, H. Singh, Preparation and coating of nano-ceramic on orthopaedic implant material using electrostatic spray deposition, Mater. Des. 88 (2015) 278–286, https://doi.org/10.1016/j.matdes.2015.08.145.
[39] M. Dehestani, E. Adolfsson, L.A. Stanciu, Mechanical properties and corrosion behavior of powder metallurgy iron-hydroxyapatite composites for biodegradable implant applications, Mater. Des. 109 (2016) 556–569, https://doi.org/10.1016/j.matdes.2016.07.092.
[40] H.R. Bakhsheshi-Rad, E. Hamzah, S.N. Saud, M. Medraj, Effect of Electrodeposition Parameters on the Microstructure and Corrosion Behavior of DCPD Coatings on Biodegradable Mg-Ca-Zn Alloy, Int. J. Appl. Ceram. Technol. 12 (2015) 1054–1064, https://doi.org/10.1111/ijac.12301.
[41] J.B. Jorcin, M.E. Orazem, N. Pébère, B. Tribollet, CPE analysis by local electrochemical impedance spectroscopy, Electrochim. Acta 51 (2006) 1473–1479, https://doi.org/10.1016/j.electacta.2005.02.128.